Submitted to: *The Astrophysical Journal*

CH 3 GHz Observations of the Galactic Center

Loris Magnani and Susan Zelenik

Department of Physics and Astronomy, The University of Georgia, Athens, GA 30602

T. M. Dame

Harvard-Smithsonian Center for Astrophysics, 60 Garden St., MS 72, Cambridge, MA 02138

and

Ben Engebreth

Colorado Center for Astrodynamics Research, University of Colorado at Boulder, Boulder, CO 80309

ABSTRACT

A 3×3 map of the Galactic Center was made at $9'$ resolution and $10'$ spacing in the CH $^2\Pi_{1/2}$, J=1/2, F=1-1 transition at 3335 MHz. The CH emission shows a velocity extent that is nearly that of the CO(1-0) line, but the CH line profiles differ markedly from the CO. The 3335 MHz CH transition primarily traces low-density molecular gas and our observations indicate that the mass of this component within ~ 30 pc of the Galactic Center is $\sim 9 \times 10^6$ $M_\odot$. The CO-H_2 conversion factor obtained for the low-density gas in the mapped region is greater than that thought to apply to the dense molecular gas at the Galactic Center. In addition to tracing the low-density molecular gas at the Galactic Center, the CH spectra show evidence of emission from molecular clouds along the line of sight both in the foreground and background. The scale height of these clouds ranges from 27 - 109 pc, consistent with previous work based on observations of molecular clouds in the inner Galaxy.

Subject headings: Galaxy: center, ISM: molecules, radio lines: ISM

1. Introduction

The Galactic Center (GC) is home to the greatest concentration of molecular gas in the Galaxy. The environment in the inner 300 pc (known as the Central Molecular Zone or CMZ) contains molecular clouds that have higher average densities and pressures than those in other regions ($n \sim 10^4$ - 10^5 cm^{-3}, $P/k \sim 10^5$ K cm^{-3} - e.g., Blitz et al. 1993; Martin et al. 2004). Most of the information on the dense molecular clouds in the CMZ has come from studies of the CO(1-0) transition and higher-density molecular mass tracers (e.g., Jackson et al. 1996; Morris 1997; Tsuboi, Handa, & Ukita 1999). However, a survey of the C^{18}O(1-0) transition in the GC region by Dahmen et al. (1998), when compared to a similar CO(1-0) survey by (Bitran et al. 1997), indicates that in addition to the dense, hot, molecular clouds, there is a molecular gas component with relatively low density ($\sim 10^{2.5}$ cm^{-3}) and high kinetic temperature ($\sim$ 150 K) whose total mass is a significant fraction of the better-studied denser component. A similar conclusion was reached by Oka et al. (1998) on the basis of CO(2-1) observations of the GC. These authors speculate that there are two components of molecular emission associated with the molecular clouds at the GC: the well-established, high-density gas arises in molecular "clumps" within the clouds that have relatively low filling factors, and a more pervasive "diffuse" component has a filling factor of $\sim$ 1. Oka et al. (1998) associate the diffuse molecular component with individual molecular clouds at the GC; for example, Sgr B2 is known to have a hot, low-density, molecular envelope (Hüttenmeister et al. 1995). However, the low-density molecular component may also be produced by the strong tidal forces at the GC that can shear clouds with densities less than a critical density (e.g., Stark & Blitz 1978; Stark & Bania 1986). In this case, the low-density gas would likely fill the volume not occupied by the dense molecular clouds and also attain a surface filling factor of $\sim$ 1. In order to survey this pervasive, diffuse, low-density molecular component, we observed 0.25 square degrees in the direction of the GC in the 3335 MHz transition of methylidine (CH).

The 3335 MHz CH line ($^2\Pi_{1/2}$, J = 1/2 ground state, F = 1-1 main-line transition) is a good linear tracer of low-density molecular gas ($n < 10^4$ cm^{-3} - Magnani et al. 2003 and references therein). Because the transition is optically thin in the interstellar medium, many of the difficulties inherent in interpreting CO(1-0) data are avoided. In addition to the molecular gas at the GC, an optically thin tracer like the 3335 MHz CH line reveals more clearly the presence of foreground and background gas along the entire line of sight. In particular, all our CH spectra show a distinct, sharp, emission feature at $v_{LSR} \sim 0$ km s^{-1}. We argue in §4 that this feature arises from molecular clouds in the near and far halves of the Galaxy whose systematic motion is perpendicular to the line of sight. The width of the feature, in turn, reflects the radial random motions of this ensemble of clouds. As a measure of the one-dimensional random motions of the cloud ensemble, the line width can be used

to determine the scale height of the molecular clouds in the beam; something that cannot be done with optically thick transitions such as the CO(1-0) line.

In this paper, we present the most sensitive CH observations of the GC to date. Unlike previous observations, the bandwidth of our observations is sufficient to cover the full velocity extent of the Galactic Center CH emission. In §2 we describe our observations and review all previous CH observations of the GC in the literature. The column densities of CH and H_2 and the molecular mass traced by the CH 3335 MHz line are derived in §3. We discuss how the CH emission compares to the CO(1-0) emission over similar velocity intervals and what the differences between the two tracers reveal about the molecular gas distribution at the GC. The value of $N(H_2)$ derived from the CH data allows us to determine the CO-H_2 conversion factor in the diffuse molecular gas, and we compare the conversion factor for the diffuse and dense components. In §4 the scale height of molecular gas along the line of sight is determined and compared to previous work. A short summary closes the paper.

2. Observations

The CH 3335 line was observed in the direction of the GC during 1999 March using the now-defunct NRAO[1] 140 ft telescope in Green Bank, West Virginia. At 3.3 GHz the beam size of the 140 ft was $9'$ which, at the distance of the GC (taken to be 8 kpc for the remainder of the paper), is 21 pc. The observing configuration consisted of a front end with a corrugated dual-hybrid mode feed in which two linear polarizations were fed into a dual-channel FET amplifier receiver. The system temperature on the sky was in the range 50 - 80 K, depending on the atmospheric conditions, the antenna elevation, and the continuum flux at 3 GHz. The autocorrelator was configured into two sections of 512 channels, with each section covering a bandwidth of 10 MHz at a velocity resolution of 1.8 km s^{-1} per channel. The total velocity coverage of each spectrum was $\sim$ 900 km s^{-1} centered on v_{LSR} = 0 km s^{-1}.

A 3 × 3 map of the GC region was made with the central spectrum at $\ell = 0°$, $b = 0°$ and all other spectra offset by 0.125° in latitude and/or longitude. Each position was observed in ON-OFF mode with one hour total on-source integrations. The OFF positions were determined from the catalog of Verter et al. (1983). For each line of sight, the two polarizations were added together and the resulting spectrum was baselined with a polynomial of order 6 (discussed in the following section) and Hann smoothed to yield an *rms* noise level of $\sim$

[1]The National Radio Astronomy Observatory (NRAO) is operated by Associated Universities, Inc., under contract with the National Science Foundation.

5-8 mK per channel. A raw spectrum for one of the lines of sight before baselining or Hann smoothing is shown in Figure 1. Baseline fitting windows were determined by looking at the raw data as in Figure 1 and by using CO spectra from Bitran et al. (1997) to indicate the maximum extent of the molecular emission. Individual reduced spectra for each position are shown in Figures 2*a* - 2*i* along with the corresponding CO(1-0) spectra from the Bitran et al. (1997) survey of the GC. The CO data are at comparable angular and velocity resolution ($8.8'$ and 1.3 km s^{-1}, respectively).

Given the historical dearth of radio telescopes with 3 GHz receivers, there are very few observations of the GC in the CH ground state, hyperfine transitions at 3 GHz. Moreover, previous observations of CH at the GC did not have sufficient sensitivity and, often, bandwidth, to detect the broad component seen in our spectra, and tended to focus on individual, narrow, emission features at the GC (Gardner & Robinson 1974; Gardner, Robinson, & Sinclair 1976; Whiteoak, Gardner, & Sinclair 1978; Genzel et al. 1979; Whiteoak et al. 1985). Thus, the extended, broad CH component described in this paper has not been noted before.

3. Results

The CH spectra presented in Figures 2*a* - 2*i* all show a velocity extent that is nearly that of the CO(1-0) emission. However, the CH line profiles look markedly different from the corresponding CO profiles. This is in contrast to the results of Magnani, Lugo, & Dame (2005) who compared CH and CO for 15 lines of sight along the Galactic plane, In those instances, the CH and CO line profiles are strikingly similar, indicating that most of the gas in these clouds is at low density. Blitz (1991) quotes an average value of Galactic plane GMCs of 50 cm^{-3}; three orders of magnitude lower than for the clouds at the GC. Given the very different nature of the molecular clouds in the plane vs. the GC, it is not surprising that in the former case the CO and CH profiles are very similar, while in the latter they are different.

However, some of the GC molecular gas *is* at low density: The widespread molecular component reported by Dahmen et al. (1998) has physical parameters ($n \sim 10^{2.5}$; T $\sim$ 150 K) ideal for CH 3 GHz observations (however, see §3.4). Following Dahmen et al. (1998) we will refer to this molecular gas as the "thin" component. The CH emission evident in Figures 2*a* -2*i* is likely tracing the thin gas and, at some level, the denser gas from GMCs in the region. Unfortunately, without extensive CH mapping of GMCs, both at the GC and elsewhere in the plane, it is not possible to determine the fraction of CH emission that arises from each component. Even though the CO and CH line profiles are different, it is not surprising that the velocity extent is similar; if tidal stripping of molecular clouds produces

the diffuse thin gas, then it likely fills the CMZ, and its velocity extent should be considerable given the GC gravitational potential. In the next section we will examine the relationship between the CO and CH emission in detail.

3.1. Comparison of velocity-integrated CO and CH

Because of the large velocity extent of the CH emission, we compare in this section the CO and CH data over similar velocity intervals. Given the complicated noncircular motions at the GC (e.g., Morris & Serabyn 1996), gas at velocities separated by only a few km s^{-1} within our 9′ beam can arise from very different regions. Thus, in order to compare emission from similar regions, we broke up each CH and CO spectrum into a series of equivalent velocity intervals. Each interval extends 9 - 10 km s^{-1} in velocity and comprises 5 or 6 channels of the CH spectra and 7 or 8 channels of the CO spectra. Despite the differing velocity resolutions, the velocity intervals were matched as closely as possible and differ by no more than 1 km s^{-1} at either extreme. In this manner, dozens of data points from each spectrum comparing the velocity-integrated antenna temperatures for both species [defined as W_{CH} and W_{CO}, respectively] can be analyzed..

The datasets at a given b for the 3 longitudes in our map are divided into positive, negative, and near 0 LSR velocities. The parameters of the best-fit line to the positive and negative data are calculated excluding the velocity interval closest to 0 km s^{-1} (i.e., the interval [−9, 0 km s^{-1}] for the negative velocities and [0, 9 km s^{-1}] for the positive velocities). The results are shown in Table 1 and reproduced in graphical form in Figure 3.

The CH emission centered on v_{LSR} = 0 km s^{-1} is composed of emission from the GC and also from foreground or background molecular gas with respect to the GC (see §4). The least squares fit to the 18 data points in this set did not show any W_{CH}-W_{CO} correlation. A glance at Figure 3 indicates that the data from this component clearly differs from the positive and negative datasets. Because the molecular gas in this dataset does not arise entirely at the GC, we will not discuss it further.

Breaking up the CH emission into $\sim$ 9 km s^{-1} intervals allows for a meaningful comparison with translucent and dark cloud data. Magnani & Onello (1995) and Magnani et al. (1998) observed CO and CH from 48 lines of sight in translucent clouds and 12 in dark clouds. The slopes of the W_{CH}-W_{CO} relation for those two data sets (8.2 and 10.1, respectively) are virtually identical to the slopes of the relation for positive and negative v_{LSR} total points in Table 1.

The results shown in Table 1 indicate that despite clear differences between the CO

and CH profiles shown in Figure 2, there is a general correlation between the CO and CH emission over similar velocity intervals. Moreover, the slope of the W_{CH} - W_{CO} relation is similar to that determined previously for a sample of local dark and translucent clouds. Similar slopes for local and GC clouds imply that the physical conditions responsible for CH 3335 MHz emission from the molecular gas at the GC are likely similar to those in local gas. This re-enforces our contention that the CH 3335 MHz emission from the GC arises primarily in low-density molecular gas - just as is the case for CH emission in local molecular clouds.

3.2. $N(H_2)$ from W_{CH} and W_{CO}

All the CH spectral profiles consist of a broad, velocity-extended component (more than 350 km s^{-1} FWZP) and a distinct spike component at $\sim$ 0 km s^{-1}. In §4 we argue that the spike feature arises from molecular gas outside the GC region. By determining the zeroth moment of the CH emission after subtracting the contribution from the 0 km s^{-1} component (determined by fitting a Gaussian to the spike), we can derive the column density of CH at the GC using the standard relationship between W_{CH} and N(CH) (Rydbeck et al. 1976). The values of W_{CH} and N(CH) for the broad component for all the observed positions are given in Table 2. The largest source of uncertainty in the analysis is produced by the baseline fit to the raw spectra. Varying the order of the polynomial used for the baseline from 4 to 8 produced variations in the integrated antenna temperature of the broad component of up to 50%, but did not change the velocity extent of the emission. With the demise of the 140 ft telescope, there is no possibility, at the moment, of re-observing the GC at 3 GHz from the Western Hemisphere in order to confirm the values of N(CH) in Table 2. Thus, the numbers we derive below are uncertain at the 50% level because of baseline uncertainties.

The relationship between N(CH) and $N(H_2)$ is linear for values of N(CH) less than 2×10^{14} cm^{-2}, corresponding to $N(H_2) \leq 5 \times 10^{21}$ cm^{-2} (Mattila 1986; Rachford et al. 2002; Magnani et al. 2003; Weselak et al. 2004). Using the relationship between E(B-V) and total hydrogen column density [Bohlin, Savage, & Drake (1978)], and a value for R_V of 3.1 (e.g., Sneden et al. 1978), a column density of 5×10^{21} cm^{-2} corresponds to a visual extinction of nearly 3 magnitudes, squarely in the translucent molecular gas regime (van Dishoeck & Black 1988). However, for $N(H_2)$ greater than 5×10^{21} cm^{-2}, the linearity of N(CH) and $N(H_2)$ begins to break down. This was evident even in the first large-scale surveys of CH (Rydbeck et al. 1976; Hjalmarson et al. 1977). Recently, using a compendium of CH data including observations from the FUSE satellite, Liszt and Lucas (2002) also note a marked decline in the CH/H_2 ratio as $N(H_2)$ increases from diffuse to dark cloud values. Moreover,

theoretical chemical models of molecular clouds invariably show that the CH abundance decreases rapidly at high extinctions or H_2 volume densities (e.g., Viala 1986; Lee, Bettens, & Herbst 1996).

The most comprehensive empirical study of the N(CH)-N(H_2) relation was conducted by Mattila (1986). Figure 10 of his paper shows a marked deviation from linearity at values of N(H_2) $> 10^{22}$ cm^{-2}. However, this deviation is based on only 6 data points from CH observations of GMCs including two lines of sight to Sgr A and Sgr B2 in the GC. The CH data for Sgr A and Sgr B2 are taken from Genzel et al. (1979) and, as mentioned in §2, do not have sufficient velocity coverage or sensitivity to reveal the CH emission in its entirety. Thus, the values of N(CH) quoted by Mattila (1986) for at least those two points are underestimated and should be considered lower limits to N(CH).

The question of how significantly the CH 3335 MHz line underestimates N(H_2) in GMCs has been addressed by Magnani, Lugo, & Dame (2005) who examined the relationship between CH and H_2 for a small sample of lines of sight through GMCs along the Galactic plane. They demonstrate that, for 10 lines of sight clustered at $(\ell, b) = (50^\circ, 0^\circ)$ and $(110^\circ, 0^\circ)$, the 3335 MHz line underestimates N(H_2) by only a factor of 2-3. This result is likely a consequence that a large fraction of a GMC's volume is composed of low-density gas (e.g., Blitz 1991; Lada, Bally, & Stark 1991).

As mentioned above, Dahmen et al. (1998) and Oka et al. (1998) have shown that not all the molecular gas at the GC is at high-density. Thus, the CH 3335 MHz line can still effectively trace some of the molecular gas. Dahmen et al. (1998) estimate that $\sim 1.0 \times 10^7$ $M_\odot$ is in the thin gas regime, while the total molecular gas mass ranges from 3.1 - 7.0 $\times 10^7$ $M_\odot$ (Sodroski et al. 1994; Blitz et al. 1985). However, these estimates are for the central 600 pc of the GC; a much larger volume than that covered by our observations. It cannot be assumed that the ratio of thin to dense gas remains constant as one nears the GC. Without knowing the fraction of thin molecular gas in the area covered by our observations, we cannot estimate the total amount of N(H_2) in the region solely on the basis of the CH data; but we can determine N(H_2) in the thin gas [defined as N$(H_2)_{\rm thin}$]. Table 2 shows that N$(H_2)_{\rm thin}$ derived from the CH observations ranges from 5.3×10^{22} to 1.5×10^{23} cm^{-2} with an average of 9.6×10^{22} cm^{-2}.

Using a distance of 8 kpc for the GC, 0.25 square degrees as the size of the observed region, and the average N(H_2) derived above, we obtain a lower limit for the thin molecular gas in the mapped region of 9×10^6 $M_\odot$.

3.3. X_{CO} at the Galactic Center

In order to obtain $N(H_2)$ from CO(1-0) data, an empirically-derived CO-H_2 conversion factor - defined as $X_{CO} = N(H_2)/W_{CO}$, where W_{CO} is the velocity-integrated CO(1-0) antenna temperature - is used. Typical values of X_{CO} in the Galactic plane range from 1.6 - 4 $\times$ 10^{20} cm^{-2} [K km s^{-1}]$^{-1}$ (e.g., Combes 1991; Strong & Mattox 1996; Hunter et al. 1997; Dame, Hartmann, & Thaddeus 2001 - we drop the units of X_{CO} for the remainder of the paper for brevity). If we use a value of 1.8 $\times$ 10^{20} as derived from far-infrared calibration mainly from the solar neighborhood by Dame, Hartmann, & Thaddeus (2001), $N(H_2)$ for the 9 CO spectra shown in Figures 2*a* - 2*i* ranges from 0.89 - 2.7 x 10^{23} cm^{-2}. However, there is strong evidence that X_{CO} at the GC is probably lower than the Galactic value.

Blitz et al. (1985) proposed a lower X_{CO} at the GC based on a deficit of gamma-rays in the region. Later, Sodroski et al. (1994) suggested, based on dust-to-gas ratio arguments, that the value of X_{CO} in the GC region is lower by a factor of 4-9 than the disk value. Similar results were found by Oka et al. (1998) and Sakano et al. (1999). Thus, instead of 1.8 $\times$ 10^{20}, X_{CO} at the GC is more likely in the 0.2 - 0.5 $\times$ 10^{20} range.

Magnani & Onello (1995) describe in detail how the CH 3335 MHz transition can be used to determine X_{CO} in translucent molecular clouds. If we apply this technique to the CH data presented here to determine $X_{CO_{\rm thin}}$, a value of 0.8 $\times$ 10^{20} is obtained. This is a lower limit because even if all the CH emission comes from $N(H_2)_{\rm thin}$, the CO(1-0) emission still arises from both the thin and the dense molecular components. If $W_{CO_{\rm dense}}/W_{CO_{\rm thin}}$ is proportional to the ratio of the mass in the thin gas to that in the dense gas, then $W_{CO_{\rm dense}}/W_{CO_{\rm thin}}$ ranges from 3-7 (see §3.2). In turn, $X_{CO_{\rm thin}}/X_{CO_{\rm dense}}$ would range over the same values.

The CH data coupled with the above argument indicate that $X_{CO_{\rm thin}}$ may be in the 2 - 6 $\times$ 10^{20} range. This result does not necessarily contradict that of Dahmen et al. (1998) who find that the lower values of X_{CO} proposed by Sodroski et al. (1994) also provide good agreement between the CO(1-0) GC mass and their estimate based on $C^{18}O$(1-0) mapping of the region. The molecular component they are referring to is the dense component. Although they derive a mass for the thin component, they do not determine what value of X_{CO} might be appropriate for it. However, they do point out that the molecular gas seen in the CO(1-0) line but not in the $C^{18}O$ transition is probably not virialized and the CO emission for this component may not be optically thick, in contrast with the dense gas in the GC GMCs. Given such disparate physical conditions for the various components of the molecular gas, usage of a single coversion factor for all the GC molecular gas is likely not valid. It may be that the best way to determine X_{CO} empirically for the thin gas is by using the CH method. The first step to address this issue would be to determine the complete extent of the CH emission from the GC region, and then to make a detailed comparison with the Bitran et

al. (1997) and Dahmen et al. (1997) data. In the section below, we discuss this type of comparison for the limited region we mapped.

3.4. Comparison of the CH 3335 MHz and $C^{18}O$ transitions

The $C^{18}O$ data used by Dahmen et al. (1998) to argue for a diffuse, warm molecular component at the GC is presented by Dahmen et al. (1997). The spectra were taken with the Southern Millimeter-Wave Telescope - just like the CO(1-0) data described above - and thus have similar spatial and velocity resolution to the CH data. The sampling of the $C^{18}O$ observations is on a slightly coarser grid than our data (0.15° vs. 0.125°), but the difference is small enough that we can make a direct comparison between our 9 CH spectra and the 9 $C^{18}O$ spectra taken by Dahmen et al. and centered on and around $(\ell, b) = (0°, 0°)$.

It is immediately clear that the velocity of the CH emission is substantially more extended than that of $C^{18}O$. For instance, the $C^{18}O$ spectrum at $(\ell, b) = (0°, -0.125°)$ shows emission only from -70 to 100 km s^{-1},[2] while the CH 3335 MHz emission clearly extends from -175 to 200 km s^{-1}. This behavior is similar for all nine CH lines of sight. Because the $C^{18}O$ directly traces the dense molecular clumps in the GMCs at the GC, it is the *absence* of $C^{18}O$(1-0) emission compared to CO(1-0) emission that led Dahmen et al. (1998) to conclude, on the basis of LVG models, that the $C^{18}O$-deficient regions likely contained warmer, lower density, molecular gas.

The CH 3335 MHz emission tracks the CO(1-0) emission in velocity very well, and indicates that the thin gas component arises predominantly in those regions that produce the most extreme velocities of molecular emission. This behavior is consistent with what would be expected from a molecular component produced by tidal stripping of gas from GMCs at the GC; this component would fill the region and rapidly assume a velocity distribution commensurate with the GC potential. In order to confirm this idea, more extensive CH mapping of the GC region should be done. At the moment, only the Parkes radiotelescope in Australia is equipped for this endeavor.

4. The Molecular Scale Height of the Galaxy

All the CH profiles show a narrow emission feature at $v_{LSR} \sim 0$ km s^{-1} . The CO data show this feature clearly only in the spectra at $b = +0.125°$. The other spectra do not

[2]The emission near -200 km s^{-1} is produced by the HNCO(5_{05} - 4_{04}) transition.

show a spike at this velocity and may even have evidence of self-absorption (cf. the spectra at $b = -0.125°$). This very different behavior of the CH 3335 MHz and CO 115 GHz line is most likely due to the very different opacities of the two transitions. The optically thin CH line is picking up emission from all the clouds along the line of sight in both the near and far halves of the Galaxy, while the CO emission at ~ 0 km s^{-1} from the GC is opaque and dominates the spectral profiles at that velocity. The CO spectra at $b = +0.125°$ show less overall CO emission than the others so the emission ~ 0 km s^{-1} is not overwhelmed and is easier to discern. Figure 4 shows the composite CH spectrum of the mapped region, and Table 3 shows the parameters of the Gaussian fits to both the composite and individual spectral profiles.

The optically thin CH spike at 0 km s^{-1} is likely sampling the emission from molecular clouds in the foreground and background with respect to the GC whose motion is primarily transverse to the line of sight. Thus, the width of the narrow feature samples the radial one-dimensional velocity dispersion of the cloud ensemble in the beam. A simple numerical simulation shows that about 2/3 of this emission arises from clouds in the near half of the Galaxy while the remainder of the emission comes from clouds beyond the GC. The simulation populates a solid angle the size of the CH beam with equivalent CH-emitting units, representing GMCs, at varying distances from the Sun. The number of units in the beam is an input parameter. Beyond a distance of 6 kpc, beam dilution decreases the contribution of each CH-emitting unit (this is equivalent to assuming that the CH-emitting units represent GMCs about 15 pc in diameter) by a factor of $(6/\mathrm{d})^2$, where d is the distance of the unit from the Sun in kpc.

Using the relation given by Magnani et al. (2000), we can calculate the scale height of the clouds in the beam given the one-dimensional velocity dispersion of the clouds, the stellar scale height, and mass surface density in the Inner Galaxy. The velocity dispersion of the clouds is readily obtained from the FWHM of the Gaussian fits to the CH narrow feature, the mass surface density is taken to be 50 ± 10 M$_\odot$ pc^{-2} (Kuijken & Gilmore 1991; Flynn & Fuchs 1994), and the stellar scale height is 300 ± 20 pc (Gilmore & Reid 1983; Binney & Merrifield 1998). With the preceding values, the molecular scale heights for the individual lines of sight vary between 27 and 73 pc (see Table 2), and for the composite profile the scale height is 109 pc. These values are similar to the values obtained from CO observations of GMCs (88 pc - Fich & Blitz 1984; 65-80 pc - Scoville & Sanders 1987; 51 pc - Bronfman et al. 1988; 74 pc - Dame et al. 1987; 35 pc - Stark and Lee 2005). The general agreement of the molecular scale height derived here with that derived from CO implies that the bulk of the molecular gas in the Galactic disk is moving on very nearly circular orbits. We do note that the scale height in the composite profile may indicate a slightly larger scale height for the molecular gas, more reminiscent of that of the local, small molecular clouds

(e.g., Magnani, Blitz, & Mundy 1985). It would be useful to probe a larger region to study the variation in linewidth of this feature as a function of position.

5. Summary

We have presented the most sensitive and velocity-extended CH 3335 MHz observations of the GC to date. The CH emission profiles cover nearly the same velocity extent as CO spectra of the corresponding regions, though the shapes of the profiles are markedly different. The values of $N(H_2)$ at the GC obtained from the CH data range from 5.3×10^{22} - 1.5×10^{23} cm^{-2}. The CH emission is likely produced by a low-density, intercloud, molecular component which pervades the GC, and a component associated with the outer envelopes of GMCs at the GC. The relative contribution from each source to the CH profile is yet to be determined.

The CO-H_2 conversion factor, X_{CO}, can be determined from the CH data for the lower density molecular component described above. The resulting value, 0.8×10^{20}, is lower than the values obtained for disk GMCs but is likely underestimated by a factor 3 - 7. This implies that X_{CO} is greater for the lower density gas than for dense GC GMCs (whose X_{CO} is thought to be in the 0.2 - 0.5 $\times$ 10^{20} range).

The mass of molecular gas within $\sim$ 30 pc of the GC as determined from the CH data is $\sim 9 \times 10^6$ $M_\odot$. Although the mapped region was fairly small ($30' \times 30'$), the CH 3335 MHz emission was readily detected for all the observed lines of sight. A more complete survey of the GC in the CH $^2\Pi_{1/2}$, J=1/2, F=0-1, 1-1, and 1-0 transitions may better trace the lower-density molecular gas than conventional CO surveys and elucidate the relation between this diffuse molecular component and atomic hydrogen at and around the GC.

An unexpected consequence of the CH survey of the GC was the detection of prominent emission at $v_{LSR} \sim 0$ km s^{-1}. This feature most likely arises from foreground and background clouds with respect to the GC and can be used to determine the scale height of this ensemble. The values we obtain (27 - 109 pc) are similar to the scale height of GMCs in the Inner Galaxy as determined from CO surveys.

Part of the work here was undertaken while S.Z. was a summer intern at the University of Georgia under a Research Experience for Undergraduates program sponsored by the National Science Foundation (PHY 00-97457). We thank Göran Sandell for a critical reading of an early version of the manuscript. We also thank an anonymous referee for comments that greatly improved the presentation of the results and the organization of the paper; in particular, with regard to the section on X_{CO}.

Table 1. CH - CO Intensity Relations - Linear Least Squares Fitting[a]

Dataset	Number of points	Intercept	Slope $\times 10^{-3}$	Correlation Coefficient
positive v_{LSR}[b]				
$\ell = 0.125°$	60	0.163	6.53	0.69
$\ell = 0.000°$	58	−0.026	9.30	0.88
$\ell = -0.125°$	41	−0.002	5.83	0.88
total	159	−0.011	8.19	0.83
negative v_{LSR}[c]				
$\ell = 0.125°$	51	0.028	22.21	0.89
$\ell = 0.000°$	43	0.327	8.36	0.53
$\ell = -0.125°$	48	0.105	3.95	0.34
total	142	0.087	9.95	0.56
non-GC gas[d]				
total	18	1.29	-1.85	-0.06

[a]In the form W_{CH} = A + B W_{CO}, where A is the y-intercept and B is the slope.

[b]Excluding data points from velocity interval $0 < v_{LSR} < 9$ km s^{-1}. See §3.1 for details.

[c]Excluding data points from velocity interval $-9 < v_{LSR} < 0$ km s^{-1}. See §3.1 for details.

[d]Includes all data points from velocity interval $-9 < v_{LSR} < +9$ km s^{-1}. See §3.1 for details.

Table 2. CH and CO Observations and Derived Quantities for the GC

ℓ degrees	b degrees	W_{CH}[a] K km s^{-1}	W_{CH}[b] K km s^{-1}	N(CH)[c] cm^{-2}	$N(H_2)_{thin}$[d] cm^{-2}	W_{CO}[e] K km s^{-1}	$N(H_2)$[f] cm^{-2}	$N(H_2)_{CO}/N(H_2)_{CH}$ [g]
0.125	0.125	8.5	7.5	2.7×10^{15}	5.7×10^{22}	888.8	1.60×10^{23}	2.8
0.125	0.000	19.2	18.3	6.5×10^{15}	13.7×10^{22}	1515.7	2.73×10^{23}	2.0
0.125	-0.125	16.5	15.3	5.4×10^{15}	11.4×10^{22}	1278.0	2.30×10^{23}	2.0
0.000	0.125	9.8	8.5	3.0×10^{15}	6.3×10^{22}	853.1	1.54×10^{23}	2.4
0.000	0.000	22.7	20.4	7.3×10^{15}	15.4×10^{22}	1472.9	2.65×10^{23}	1.7
0.000	-0.125	18.0	16.0	5.7×10^{15}	12.0×10^{22}	1032.6	1.86×10^{23}	1.6
-0.125	0.125	8.3	6.9	2.5×10^{15}	5.3×10^{22}	494.0	8.89×10^{22}	1.7
-0.125	0.000	9.6	8.0	2.9×10^{15}	6.1×10^{22}	1171.3	2.11×10^{23}	3.5
-0.125	-0.125	15.3	14.0	5.0×10^{15}	10.5×10^{22}	1237.2	2.23×10^{23}	2.1

[a]Velocity-integrated CH 3335 MHz antenna temperature. The uncertainty in this quantity is driven overwhelmingly by the baseline fit (see §3.2

[b]Velocity-integrated CH 3335 MHz antenna temperature for the broad, extended component only (see §3).

[c]N(CH) is derived from the integrated antenna temperature in column 3 after correcting for the beam efficiency, the beam filling fraction, and assuming $| T_{ex}| \gg T_{bg}$. See Magnani & Onello (1995) for details.

[d]$N(H_2)$ derived from N(CH) via the relation established by Mattila (1986). We refer to this gas as "thin" for reasons elaborated in §3.2

[e]Integrated CO(1-0) line emission from the data of Bitran et al. (1997).

[f]$N(H_2)$ derived from W_{CO} using a conversion factor of 1.8×10^{20}.

[g]Ratio of $N(H_2)$ derived from CO(1-0) data divided by $N(H_2)$ derived from CH data.

Table 3. The CH Narrow Component at $v_{LSR} \sim 0$ km s^{-1}

ℓ degrees	b degrees	T_A mK	Δv km s^{-1}	v_{LSR} km s^{-1}	Scale Height [a] pc
0.125	0.125	115	8.41	−0.31	54
0.125	0.000	213	4.26	+1.66	27
0.125	-0.125	104	11.38	−3.08	73
0.000	0.125	230	5.40	−0.13	34
0.000	0.000	270	7.76	−0.25	49
0.000	-0.125	167	11.34	−4.46	72
-0.125	0.125	186	7.05	−1.76	45
-0.125	0.000	137	10.54	−0.49	67
-0.125	-0.125	111	10.62	−3.40	68
composite [b]		182	17.61	−1.20	109

[a]Scale height is derived using formulation given by Magnani et al. (2000 - see §4 for details).

[b]Average of the 9 individual spectra. See Figure 4.

REFERENCES

Binney, J. & Merrifield, M. 1998, *Galactic Astronomy* (Princeton: Princeton Univ. Press)

Bitran, M., Alvarez, H., Bronfman, L., May, J., & Thaddeus, P. 1997, A&AS, 125, 99

Blitz, L., Bloemen, J.B.G.M., Hermsen, W., & Bania, T.M. 1985, ApJ, 143, 267

Blitz, L. 1991, in The Physics of Star Formation and Early Stellar Evolution, ed. C.J. Lada & N.D. Kylafis (Dordrecht: Kluwer), 3

Blitz, L., Binney, J., Lo, K.Y., Bally, J., & Ho, P.T.P. 1993, Nature, 361, no. 6411, 417

Bloemen, J.B.G.M. 1986, A&A, 154, 25

Bohlin, R.C., Savage, B.D., & Drake, J.F. 1978, ApJ, 224, 132

Bronfman, L. 1988, ApJ, 324, 248

Combes, F. 1991, ARA&A, 29, 195

Dahmen, G., et al. 1997, A&AS, 126, 197

Dahmen, G., Hüttemeister, S., Wilson, T.L., & Mauersberger, R. 1998, ApJ, 331, 959

Dame, T.M. et al. 1987, ApJ, 322, 706

Dame, T.M., Hartmann, D., & Thaddeus, P. 2001, ApJ, 547, 792

Federman, S. R. 1982, ApJ, 257, 125

Fich, M. & Blitz, L. 1984, ApJ, 279, 125

Flynn, C. & Fuchs, B. 1994, MNRAS, 202, 1025

Gardner, F.F. & Robinson, B.J. 1974, PASAu, 2, 253

Gardner, F.F., Robinson, B.J., & Sinclair, M.W. 1976, AuJPh, 29, 211

Genzel, R., Downes, D., Pauls, T., Wilson, T.L., & Bieging, J. 1979, A&A, 73, 253

Gilmore, G. & Reid, N. 1983, MNRAS, 202, 1025

Hjalmarson, Å. et al. 1977, ApJS, 35, 263

Hunter, S.D. et al. 1997, ApJ, 481, 205

Hüttenmesiter, S., Wilson, T.L., Mauersberger, R., Lemme, C., Dahmen, G., & Henkel. C. 1995, A&A, 294, 667

Jackson, J.M., Heyer, M.H., Paglione, T.A.D., & Bolatto, A.D. 1996, ApJ, 456, 91

Kuijken, K. & Gilmore, G. 1989, MNRAS, 239, 605

Lada, E.A., Bally, J., & Stark, A.A. 1991, ApJ, 368, 432

Lee, H.-H., Bettens, R.P.A., & Herbst, E. 1996, A&AS, 119, 111

Liszt, H. & Lucas, R. 2002, A&A, 391, 693

Magnani, L., Blitz, L., & Mundy, L. 1985, ApJ, 295, 402

Magnani, L. & Onello, J.S. 1995, ApJ, 443, 169

Magnani, L., Hartmann, D., & Speck, B.G. 1996, ApJS, 106, 447

Magnani, L., Onello, J.S., Adams, N.G., Hartmann, D., & Thaddeus, P. 1998, ApJ, 504, 290

Magnani, L., Hartmann, D., Holcomb, S.L., Smith, L.E., & Thaddeus, P. 2000, ApJ, 535, 167

Magnani, L., Chastain, R.J., Kim, H.C., Hartmann, D., Truong, T., & Thaddeus, P. 2003, ApJ, 586, 1111

Magnani, L., Lugo, S., & Dame, T.M. 2005, AJ, submitted

Martin, C.L., Walsh, W.M., Xiao, K., Lane, A.P., Walker, C.K., & Stark, A.A. 2004, ApJS, 150, 239

Mattila, K. 1986, A&A, 160, 157

Morris, M. 1997, in *CO: Twenty-Five Years of Millimeter-Wave Spectroscopy*, W.B. Latter et al. (eds.), (Dordrecht: Reidel), 57

Morris, M. & Serabyn, E. 1996, ARA&A, 645, 701

Oka, T., Hasegawa, T., Hayashi, M., Handa, T., & Sakamoto, S. 1998, ApJ, 493, 730

Rachford, B.L. et al. 2002, ApJ, 577, 221

Rydbeck, O.E.H., Kollberg, E., Hjalmarson, Å., Sume, A., & Elldér, J. 1976, ApJS, 31, 333

Sakano, M., Koyama, K., Nishiuchi, M., Yokogawa, J., & Maeda, Y. 1999, Adv. Space Res., 23, 969

Scoville, N.Z. & Sanders, D.B. 1987, in *Interstellar Processes*, ed. D.J. Hollenbach & H.A. Thronson, Jr. (Dordrecht, Reidel), 21

Sneden, C., Gehrz, R.D., Hackwell, J.A., York, D.G., & Snow, T.P. 1978, ApJ, 223, 168

Sodroski, T. et al. 1994, ApJ, 428, 638

Stark, A.A. & Blitz, L. 1978, ApJ, 225, L15

Stark, A.A. & Bania, T.M. 1986, ApJ, 306, L17

Stark, A.A. & Lee, Y. 2005, ApJ, 619, L159

Strong, A.W. et al. 1988, A&A, 207, 1

Strong, A.W. & Mattox, J.R. 1996, A&A, 308, L21

Tsuboi, M., Handa, T., & Ukita, N. 1999, ApJS, 120, 1

Ungerechts, H., Umbanhowar, P., & Thaddeus, P. 2000, ApJ, 537, 221

van Dishoeck, E.F. & Black, J.H. 1988, ApJ, 334, 771

Verter, F., Knapp, G.R., Stark, A.A., & Wilson, R.W. 1983, ApJS, 52, 289

Viala, Y.P. 1986, A&AS, 64, 391

Weselak, T., Galazutdinov, G.A., Musaev, F.A., & Krelowski, J. 2004, A&A, 949

Whiteoak, J.B., Gardner, F.F., & Sinclair, M.W. 1978, MNRAS, 184, 235

Whiteoak, J.B., Gardner, F.F., Manefield, G.A., Höglund, B., & L.E.B. Johansson 1985, PASAu, 6, 6

Fig. 1.— Raw CH spectrum at one of the 9 positions ($\ell = 0.000°$, $b = 0.125°$). The spectrum is a one-hour on source integration on in ON-OFF mode, with both polarizations added together. Emission is present from at least -100 to $+180$ km s^{-1}. See §2 for more details. The same data are presented after Hann smoothing and removal of a sixth order baseline in the lower panel of Figure 2d.

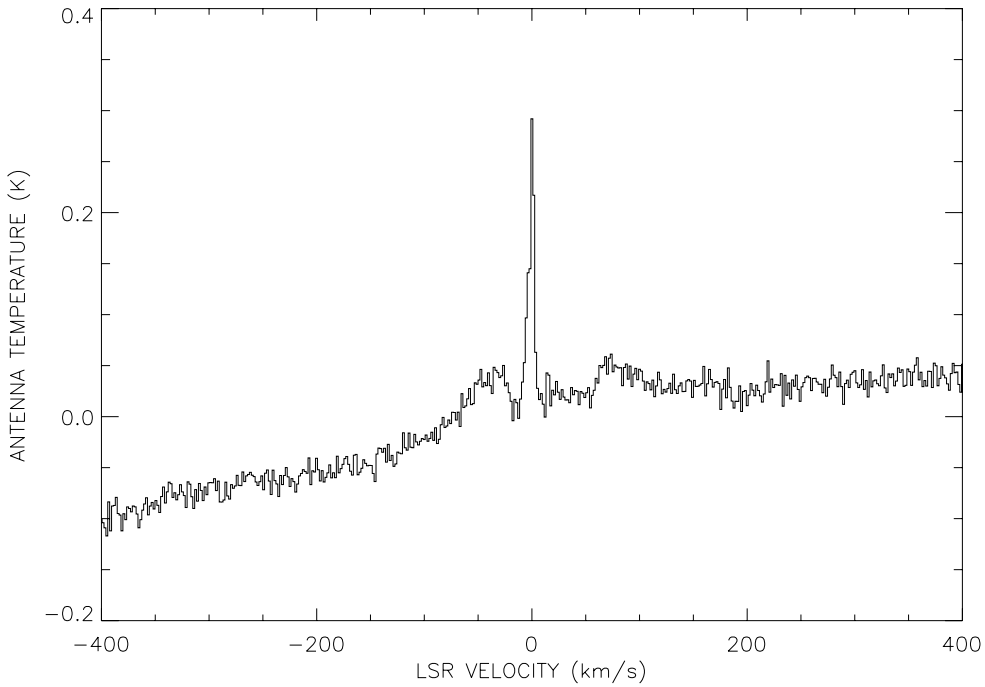

Fig. 2a.— CH and CO spectra for each of the nine observed lines of sight. At bottom, spectrum of the CH $^2\Pi_{1/2}$ F=(1-1) transition at 3335 MHz for position $\ell = 0.125°$, $b = 0.125°$. The beamsize is $9'$ and the velocity resolution is 3.6 km s^{-1} after Hann smoothing. Above, CO(1-0) spectrum from Bitran et al. (1997) for the same position with a beamsize of $8.8'$ and a velocity resolution of 1.3 km s^{-1}. See §2 for more details.

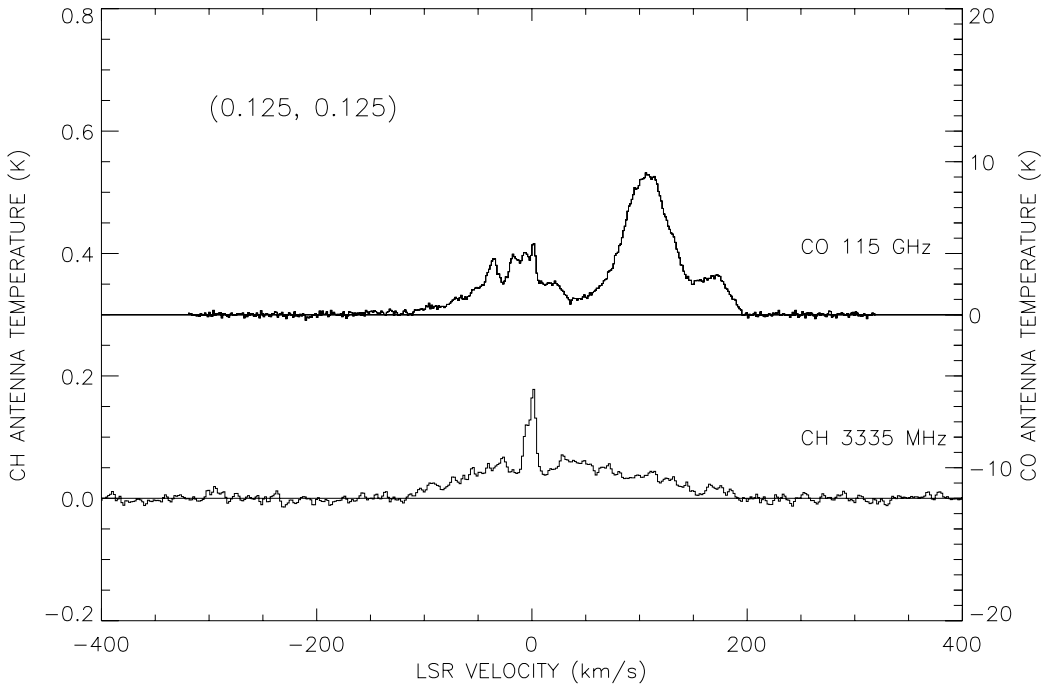

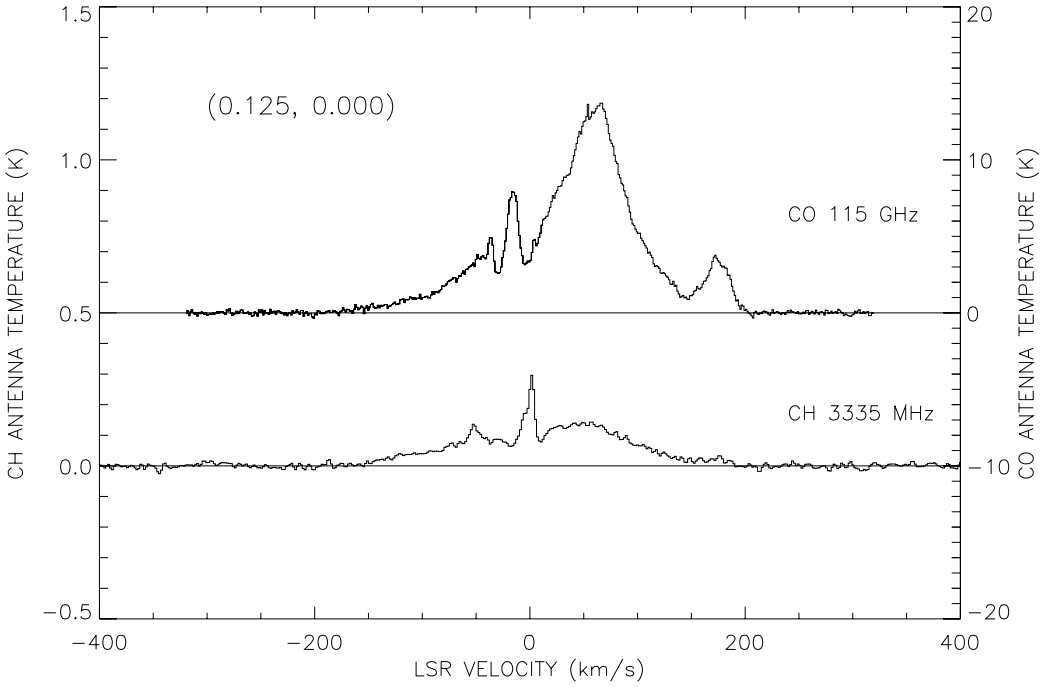
(0.125, 0.000)
CO 115 GHz
CH 3335 MHz
CH ANTENNA TEMPERATURE (K)
CO ANTENNA TEMPERATURE (K)
LSR VELOCITY (km/s)
1.5
1.0
0.5
0.0
−0.5
20
10
0
−10
−20
−400
−200
0
200
400

Fig. 2b.—

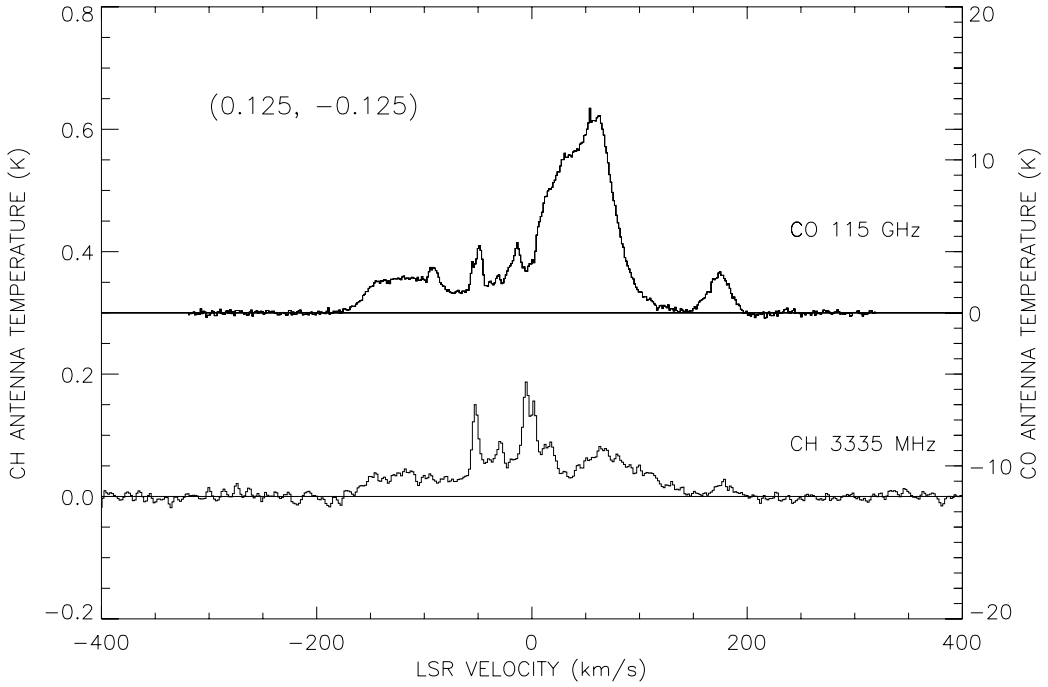
(0.125, −0.125)
CO 115 GHz
CH 3335 MHz
CH ANTENNA TEMPERATURE (K)
CO ANTENNA TEMPERATURE (K)
LSR VELOCITY (km/s)
0.8
0.6
0.4
0.2
0.0
−0.2
20
10
0
−10
−20
−400
−200
0
200
400

Fig. 2c.—

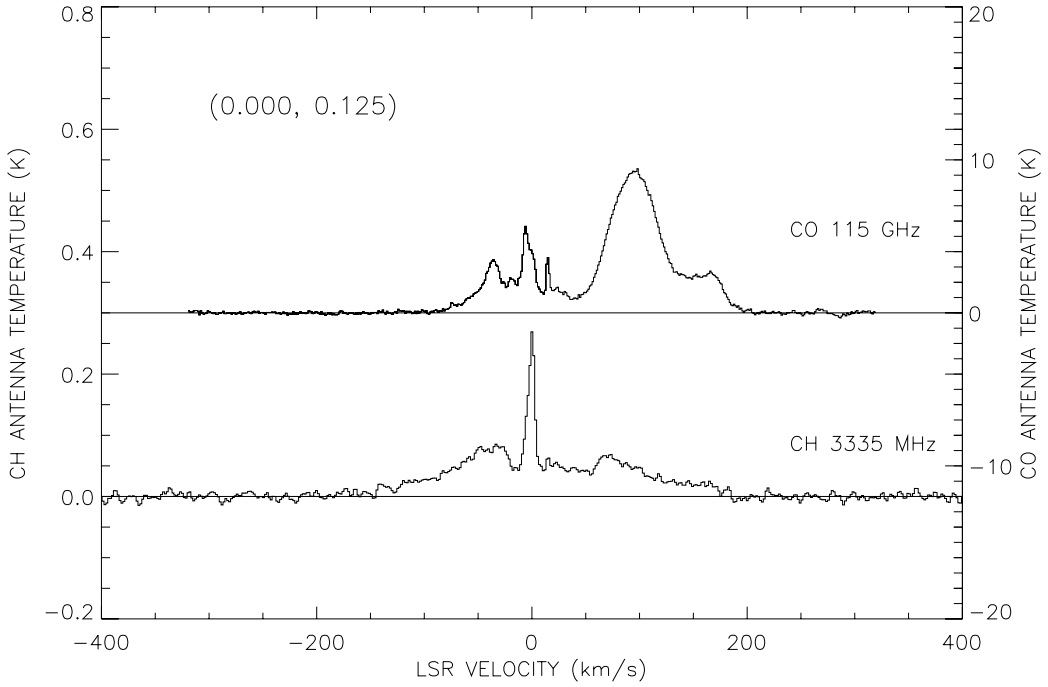
(0.000, 0.125)
CO 115 GHz
CH 3335 MHz
CH ANTENNA TEMPERATURE (K)
CO ANTENNA TEMPERATURE (K)
LSR VELOCITY (km/s)
0.8
0.6
0.4
0.2
0.0
−0.2
20
10
0
−10
−20
−400
−200
0
200
400

Fig. 2d.—

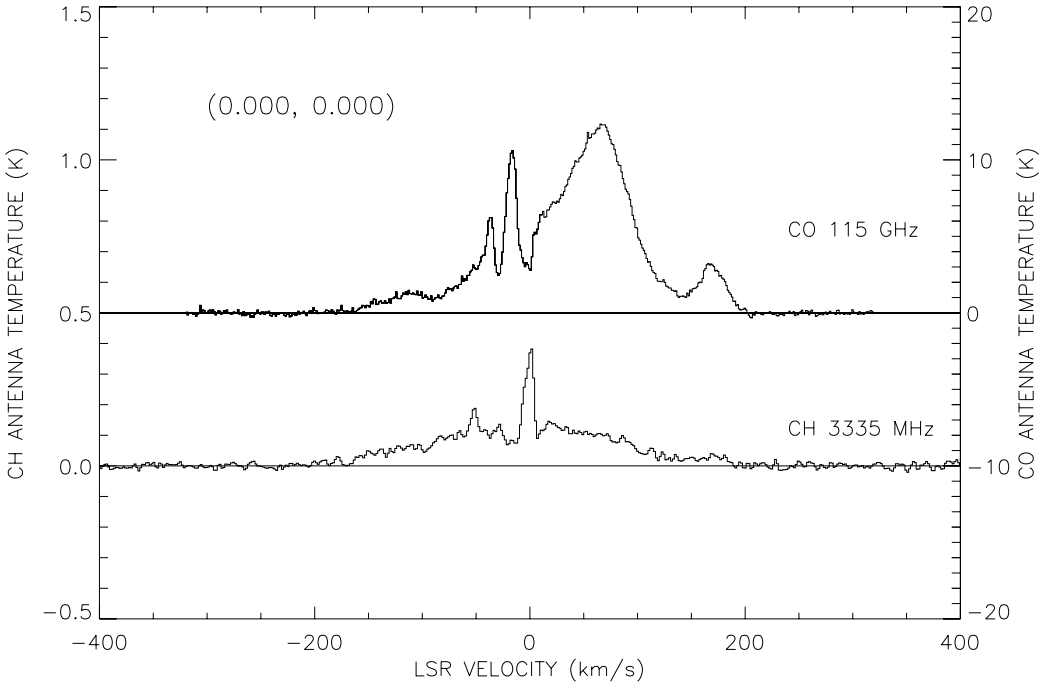
(0.000, 0.000)
CO 115 GHz
CH 3335 MHz
CH ANTENNA TEMPERATURE (K)
CO ANTENNA TEMPERATURE (K)
LSR VELOCITY (km/s)
1.5
1.0
0.5
0.0
−0.5
20
10
0
−10
−20
−400
−200
0
200
400

Fig. 2e.—

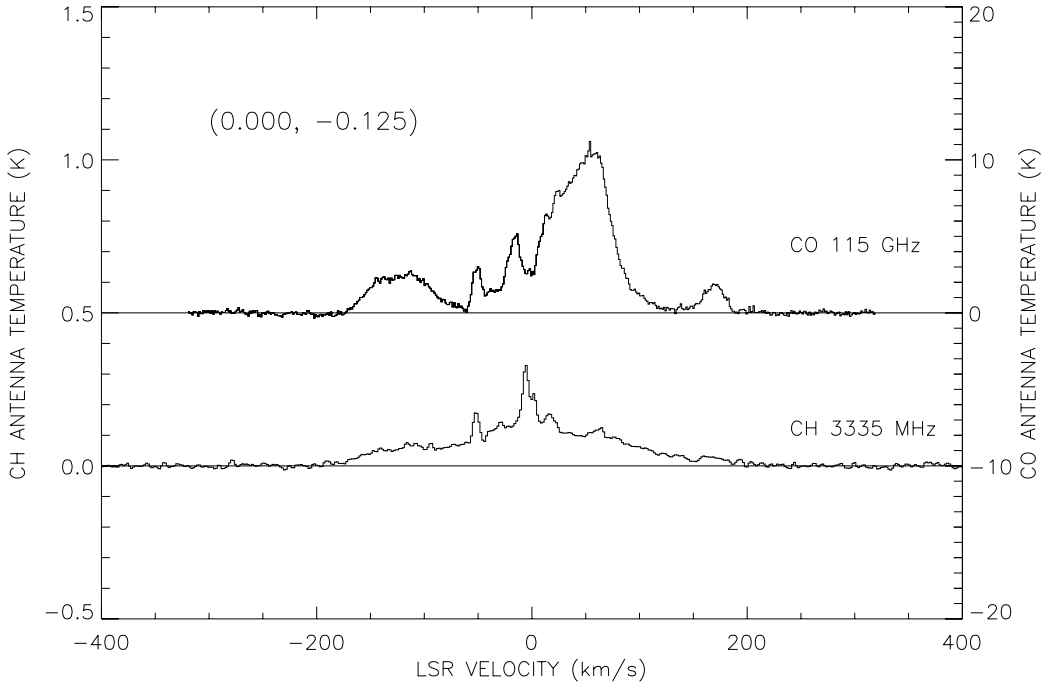
(0.000, −0.125)
CO 115 GHz
CH 3335 MHz
CH ANTENNA TEMPERATURE (K)
CO ANTENNA TEMPERATURE (K)
LSR VELOCITY (km/s)
1.5
1.0
0.5
0.0
−0.5
20
10
0
−10
−20
−400
−200
0
200
400

Fig. 2f.—

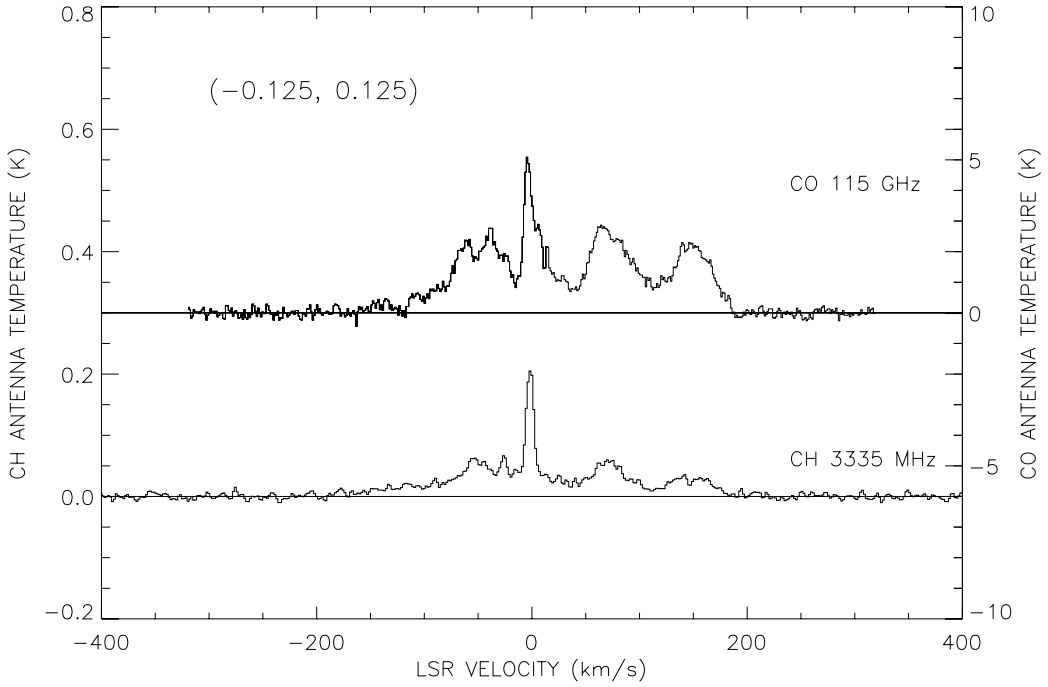
(−0.125, 0.125)
CO 115 GHz
CH 3335 MHz
CH ANTENNA TEMPERATURE (K)
CO ANTENNA TEMPERATURE (K)
LSR VELOCITY (km/s)
0.8
0.6
0.4
0.2
0.0
−0.2
10
5
0
−5
−10
−400
−200
0
200
400

Fig. 2g.—

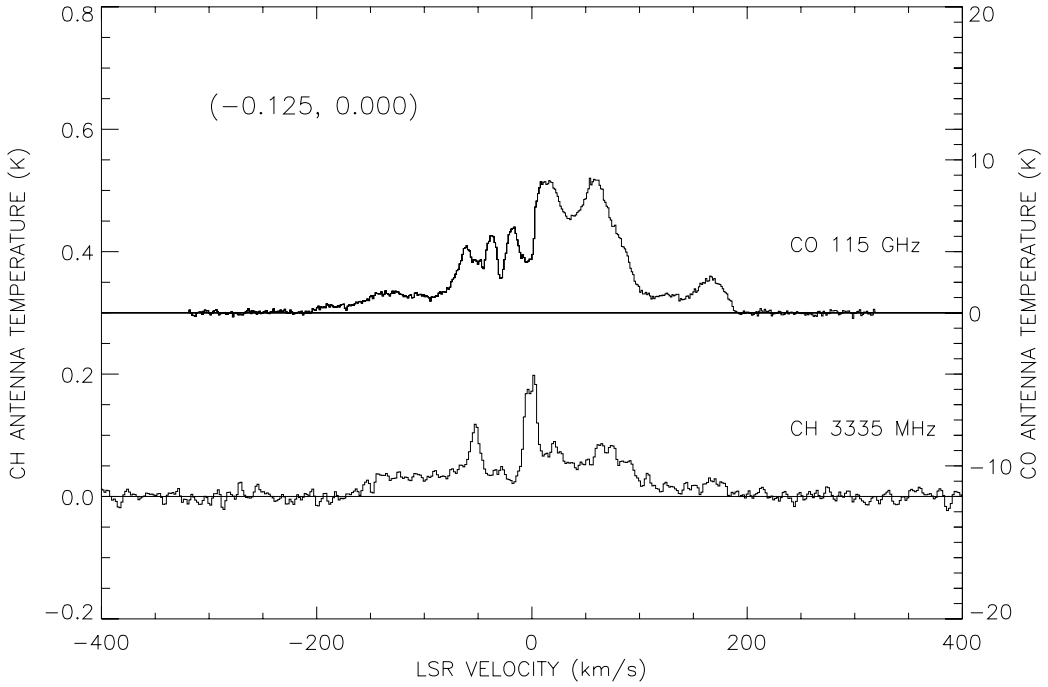
(−0.125, 0.000)
CO 115 GHz
CH 3335 MHz
CH ANTENNA TEMPERATURE (K)
CO ANTENNA TEMPERATURE (K)
LSR VELOCITY (km/s)
0.8
0.6
0.4
0.2
0.0
−0.2
20
10
0
−10
−20
−400
−200
0
200
400

Fig. 2h.—

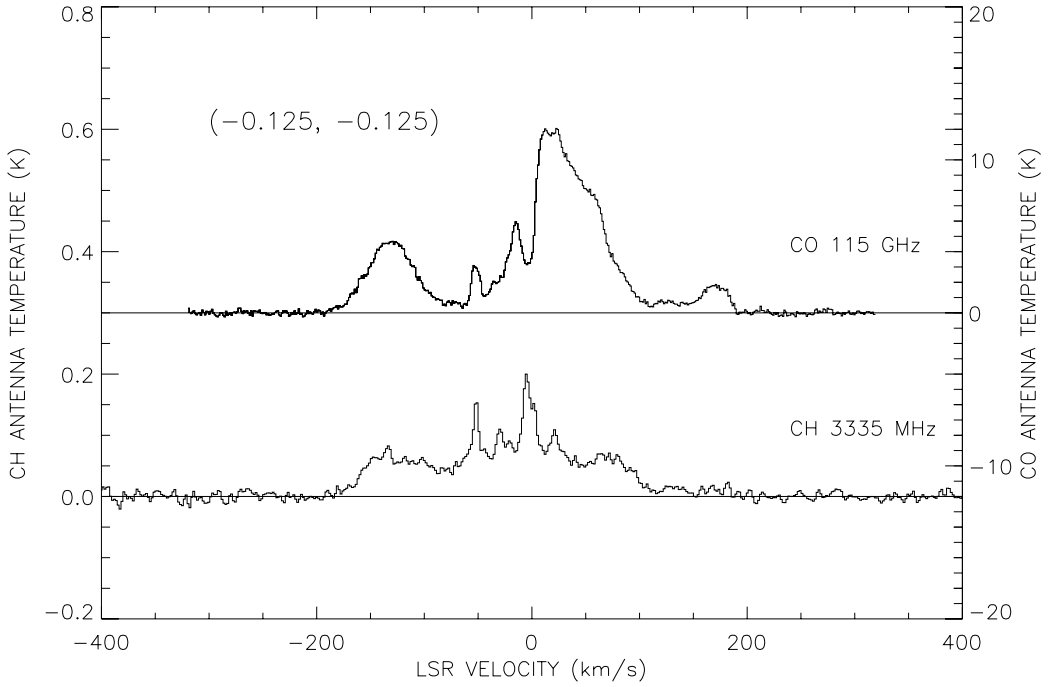
(−0.125, −0.125)
CO 115 GHz
CH 3335 MHz
CH ANTENNA TEMPERATURE (K)
CO ANTENNA TEMPERATURE (K)
LSR VELOCITY (km/s)
0.8
0.6
0.4
0.2
0.0
−0.2
20
10
0
−10
−20
−400
−200
0
200
400

Fig. 2i.—

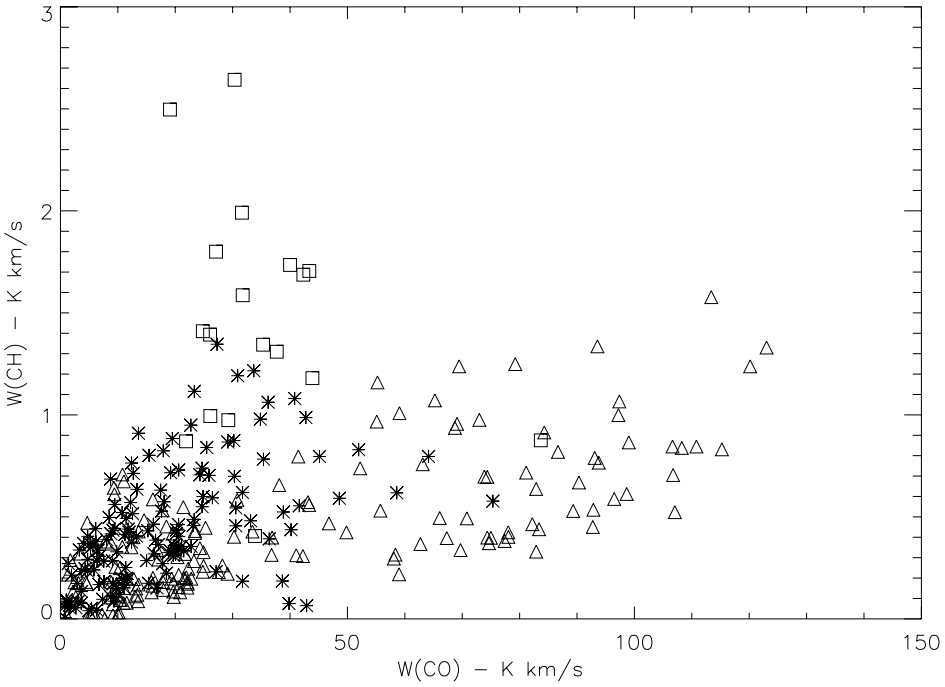

Fig. 3.— Plot of W_{CH} (the velocity-integrated antenna temperature) versus W_{CO} for all the data in the mapped region binned in velocity intervals of ~ 9 km s^{-1}. The data are broken up into 3 subsets: the triangles represent positive velocity intervals greater than 9 km s^{-1}, the asterisks represent negative velocity intervals less than -9 km s^{-1}, and the squares represent

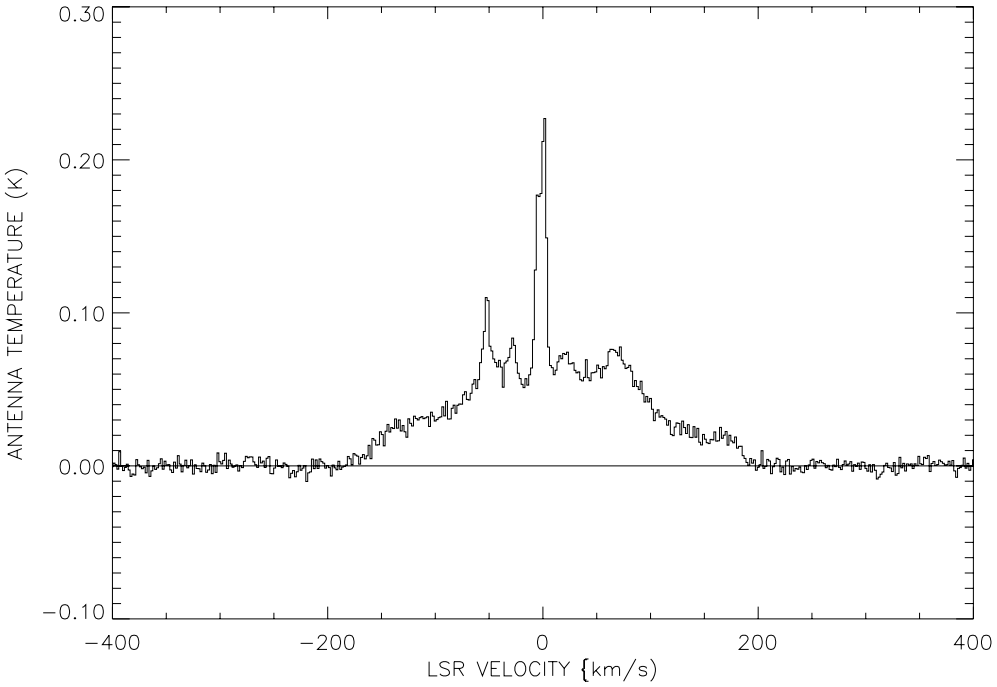

Fig. 4.— Averaged CH spectrum of the mapped region. The strong, narrow emission at ~ 0 km s^{-1} is evident and a Gaussian fit to it gives a FWHM of 17.6 km s^{-1} centered at $v_{LSR} = -1.20$ km s^{-1} (see §4 for details). Also noticeable is the emission from the 3-kpc arm at v ~ -50 km s^{-1}.